

Coherent Rydberg excitation of single atoms using a pulsed fiber amplifier

Ying-Wen Zhang(张应文), Yang Wang(王洋), Chen-Long Xu(徐晨龙), Yi-Bo Wang(王一波), and Peng Xu(许鹏)
Citation: Chin. Phys. B, 2026, 35 (**8**): 083204. DOI: 10.1088/1674-1056/ae5db3
http://cpb.iphy.ac.cn; http://iopscience.iop.org/cpb

What follows is a list of articles you may be interested in

Co-optimization of linear gain and dynamic range for atomic superheterodyne receivers based on homodyne readout

Chuan Qu(瞿川), Dongqin Guo(郭东琴), and Jian Zhang(张剑)
Chin. Phys. B, 2026, 35 (**1**): 013202. DOI: 10.1088/1674-1056/ade8e9

Polarization impact on sensitivity of Rydberg atom-based microwave sensors

Minghao Cai(蔡明皓), Aomao Wei(魏奥贸), Shanshan Chen(陈珊珊), and Yuming Huang(黄聿铭)
Chin. Phys. B, 2025, 34 (**8**): 083201. DOI: 10.1088/1674-1056/add005

Optimization strategies for operational parameters of Rydberg atom-based amplitude modulation receiver

Yuhao Wu(吴宇豪), Dongping Xiao(肖冬萍), Huaiqing Zhang(张淮清), and Sheng Yan(阎晟)
Chin. Phys. B, 2025, 34 (**1**): 013201. DOI: 10.1088/1674-1056/ad886a

Microwave field sensor based on cold cesium Rydberg three-photon electromagnetically induced spectroscopy

Yuan-Yuan Wu(吴圆圆), Yun-Hui He(何云辉), Yue-Chun Jiao(焦月春), and Jian-Ming Zhao(赵建明)
Chin. Phys. B, 2024, 33 (**11**): 113201. DOI: 10.1088/1674-1056/ad7579

Atom-based power-frequency electric field measurement using the radio-frequency-modulated Rydberg spectroscopy

Weixin Liu(刘伟新), Linjie Zhang(张临杰), and Tao Wang(汪涛)
Chin. Phys. B, 2023, 32 (**5**): 053203. DOI: 10.1088/1674-1056/aca6db

---

SPECIAL TOPIC — Quantum frontiers with Rydberg atoms

Coherent Rydberg excitation of single atoms using a pulsed fiber amplifier

Ying-Wen Zhang(张应文)[1], Yang Wang(王洋)[2,3], Chen-Long Xu(徐晨龙)[2,3], Yi-Bo Wang(王一波)[2,†], and Peng Xu(许鹏)[2,4]

[1] *School of Mathematics and Physics, China University of Geosciences, Wuhan* 430074, *China*
[2] *Division of Precision Measurement Physics, Innovation Academy for Precision Measurement Science and Technology, Chinese Academy of Sciences, Wuhan* 430071, *China*
[3] *School of Physical Sciences, University of Chinese Academy of Sciences, Beijing* 100049, *China*
[4] *Wuhan Institute of Quantum Technology, Wuhan* 430206, *China*

(Received 9 February 2026; revised manuscript received 30 March 2026; accepted manuscript online 10 April 2026)

In recent years, the growing scale of programmable neutral-atom arrays has led to an increasing demand for higher-power Rydberg excitation light. Although pulsed amplifiers deliver higher peak power than continuous-wave lasers, their application to efficient coherent Rydberg excitation of single atoms in arrays has been limited by challenges such as pulse distortion, synchronization with excitation sequences, and spectral linewidth broadening. Here, we address these issues using a fiber-based master-oscillator power-amplifier system. We demonstrate efficient coherent Rydberg excitation of single atoms in a rubidium atom array, achieving performance comparable to that of continuous-wave methods. This study provides a new technical pathway toward future large-scale quantum simulation and computation with Rydberg atom arrays.

Keywords: single atoms, coherent Rydberg excitation, pulsed fiber amplifier, waveform pre-shaping

PACS: 32.80.Ee, 42.60.Fc, 03.67.Lx, 32.80.Qk

DOI: 10.1088/1674-1056/ae5db3 **CSTR:** 32038.14.CPB.ae5db3

1. Introduction

Neutral-atom arrays have rapidly developed into a leading platform for realizing programmable quantum systems. In this approach, individual cold atoms are trapped in arrays of optical tweezers, and controllable interactions are introduced by exciting the atoms to Rydberg states. The system exhibits excellent qubit coherence,[1,2] scalability,[3,4] flexible qubit connectivity,[5] high-fidelity Rydberg excitation control,[6] and two-qubit logic gates.[7–9] It has been successfully used to prepare complex quantum many-body states[10–12] and provides an experimental testbed for constructing scalable architectures toward universal fault-tolerant quantum computing.[13,14]

To advance quantum simulation and computation, experimental systems are being progressively scaled up,[15,16] placing higher demands on experimental control — particularly the need for higher-power Rydberg excitation light to address larger atom arrays and achieve faster Rabi frequencies.[8] For example, in rubidium atoms, the 420 nm + 1013 nm two-photon excitation scheme is widely adopted, largely because readily available near-infrared continuous-wave (CW) lasers — such as Ti:sapphire and fiber lasers delivering tens to hundreds of watts — can efficiently drive the upper transition from the intermediate state to the Rydberg state, despite its small transition dipole moment. In neutral-atom-array experiments, the excitation sequence typically operates in a pulsed mode: the Rydberg excitation light is switched on only during short windows (typically on the order of microseconds) via components such as acousto-optic modulators (AOMs) and remains off otherwise. In such a pulsed configuration, the attainable peak power remains limited by the available CW laser power.

In contrast, pulsed lasers concentrate energy within extremely short time windows, delivering peak powers significantly higher ($>$ 1 kW) than those of CW sources.[17–19] This characteristic makes them a compelling alternative to CW lasers for supplying higher-power Rydberg excitation. Previous studies have utilized picosecond pulses for ultrafast Rydberg excitation[20] and nanosecond pulses for electromagnetically induced transparency (EIT) spectroscopy.[21] However, efficient coherent excitation of single atoms with microsecond pulsed lasers remains elusive due to challenges such as severe pulse distortion,[22,23] synchronization with excitation sequences, and spectral linewidth broadening.

In this paper, we implement a fiber-based master-oscillator power-amplifier (MOPA) scheme to achieve efficient coherent Rydberg excitation of single atoms in a rubidium atom array. We address waveform distortion and pulse-sequence synchronization. The demonstrated performance is comparable to that of continuous-wave methods, indicat-

[†]Corresponding author. E-mail: wangyb@apm.ac.cn

© 2026 Chinese Physical Society and IOP Publishing Ltd. All rights, including for text and data mining, AI training, and similar technologies, are reserved.

ing that the MOPA architecture largely preserves the narrow linewidth of the seed laser during power amplification. This work thus provides a potentially new technical route toward scalable, high-fidelity Rydberg-based quantum control. The rest of this paper is organized as follows. Section 2 describes the pre-shaping of the 1013 nm seed-pulse waveform to suppress amplified pulse distortion. In Section 3, we synchronize the selected amplified 1013 nm pulse with a 420 nm pulse generated from a CW laser to drive coherent Rydberg excitation of single atoms in a rubidium atom array and compare the results with those obtained using a conventional CW scheme. Finally, Section 4 summarizes the main findings and discusses potential applications of the pulsed fiber amplifier scheme.

2. Pulse pre-shaping compensates for waveform distortion during amplification

In the experiment, a pulsed fiber amplifier module (Connet MFAP-Yb-1013-M-SF) with a peak power of 50 W is employed to amplify the input 1013 nm seed laser. This amplifier utilizes an ytterbium-doped fiber as the gain medium, with pump light establishing the initial population inversion between the upper and lower energy levels of the Yb^{3+} ions. The seed laser, first modulated by an AOM to generate optical pulses with tunable pulse width and repetition rate, is then introduced into the gain medium. Within the fiber, photons from the seed pulse stimulate the excited Yb^{3+} ions to return to the ground state, emitting additional photons through stimulated emission and thereby amplifying the pulse.

During the amplification process, the leading edge of the pulse first enters the gain medium, where the population inversion has not yet been depleted, resulting in high gain and strong amplification. As the pulse propagates through the medium, the population inversion is progressively depleted. By the time the trailing edge arrives, the gain decreases, leading to weaker amplification.[22,23] This variation causes distortion in the output pulse waveform. Figure 1 illustrates this phenomenon using a square input pulse as an example. The input waveform is shown in Fig. 1(a), while the black curve in Fig. 1(b) represents the experimental output waveform. It can be seen that the output waveform exhibits significant distortion due to gain saturation.

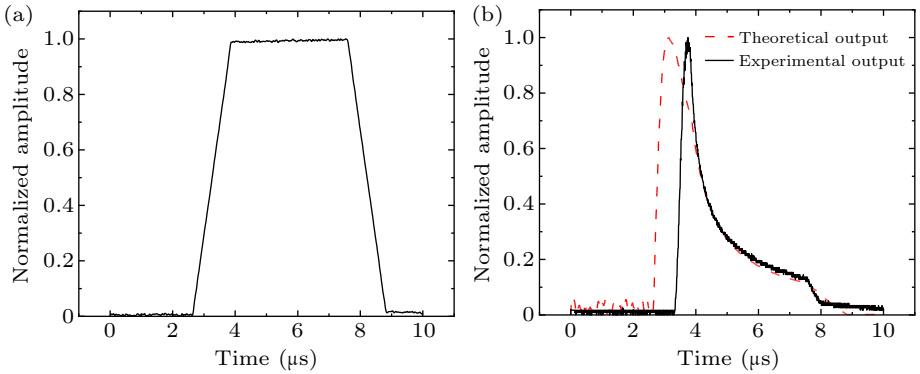


Fig. 1. Shapes of the input and output pulses. (a) Input RF driving pulse. (b) Output pulse. The black and red curves denote the experimental and theoretical output waveforms, respectively. The amplifier module is operated at a pump power of 3 W and a repetition rate of 2 kHz.

The dynamic evolution of the photon density of the pulse and the population inversion during amplification can be quantitatively described by the Frantz–Nodvik equation[23]

$$n(z,t) = n_0\left(t-\frac{z}{c}\right)\left\{1-\left[1-\exp\left(-\sigma\int_0^z \Delta_0(z')\,\mathrm{d}z'\right)\right] \times \exp\left(-2\sigma c\int_{-\infty}^{t-\frac{z}{c}} n_0(t')\,\mathrm{d}t'\right)\right\}^{-1}, \quad (1)$$

where n denotes the photon number density, σ is the stimulated emission cross-section, c represents the speed of light in the medium, and Δ_0 denotes the initial population inversion. Furthermore, we can derive the expression for the output pulse $I_{s,z}(T)$ after an input pulse $I_{s,0}(T)$ passes through a fiber of length L, given by

$$I_{s,z}(T) = \frac{I_{s,0}(T)}{1-\left(1-G_0^{-1}(z)\right)\exp\left(-J_{\mathrm{sat}}^{-1}\int_{-\infty}^{T} I_{s,0}(t')\,\mathrm{d}t'\right)}, \quad (2)$$

where I is the optical intensity, $T = t - z/c$, $G_0(z) = \exp\left(\sigma\int_0^z \Delta_0(z')\,\mathrm{d}z'\right)$ is the small-signal gain, $J_{\mathrm{out}}(T) = \int_{-\infty}^{T} I_{s,0}(t')\,\mathrm{d}t'$ represents the output pulse fluence, and J_{sat} is the saturation fluence, given by $h\nu/(2\sigma)$. At the onset of amplification, $J_{\mathrm{out}} = 0$, the denominator equals $1/G_0$, and the gain is G_0. As amplification proceeds, J_{out} increases, causing the denominator to increase and the gain to gradually decrease. When $J_{\mathrm{out}} \gg J_{\mathrm{sat}}$, the denominator approaches unity, at which point the gain drops to 1, indicating that the gain is fully saturated and no further power amplification occurs.

Based on this model, the correspondence between the input and output waveforms can be readily established. Taking the measured waveform in Fig. 1(a) as the input, we adjust the two undetermined parameters in Eq. (2), namely the initial population inversion and the stimulated emission cross-section, so that the theoretically calculated output waveform progressively approaches the measured output waveform. This

process determines the values of these parameters. As indicated by the red curve in Fig. 1(b), the theoretical waveform shows good overall agreement with the measured one. The main discrepancy is that the theoretical waveform is slightly broader than the measured one. This difference arises because the actual amplification process is accompanied by temporal pulse compression,[24] an effect not accounted for in the theoretical calculation.

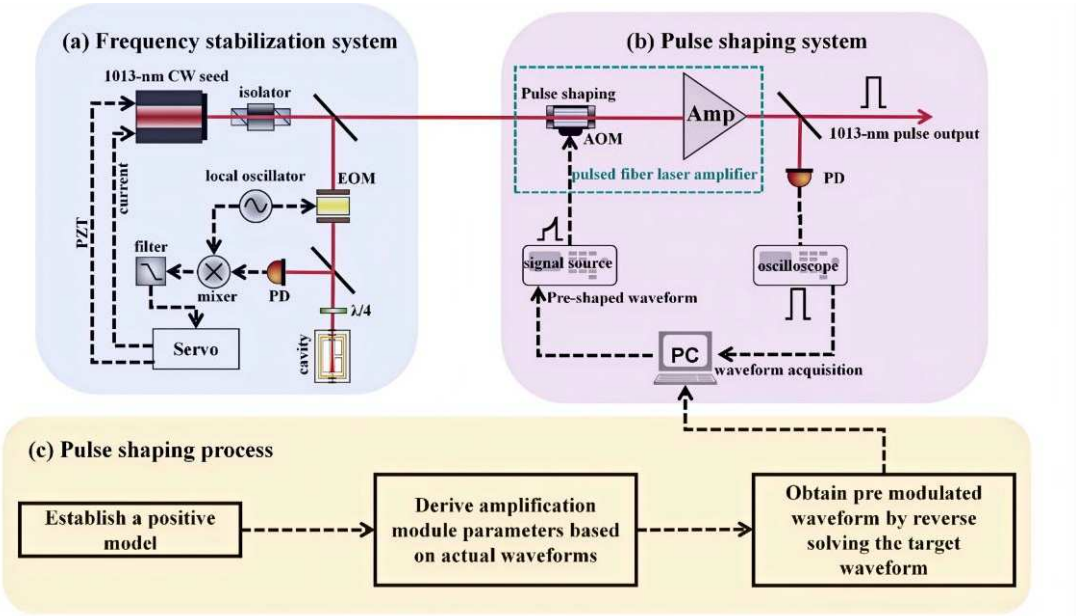


Fig. 2. Pulse waveform pre-shaping scheme. (a) Optical setup for Pound–Drever–Hall (PDH) locking of the laser to an ultra-stable cavity. (b) Schematic diagram of the pulse-shaping system. (c) Pulse waveform pre-shaping process.

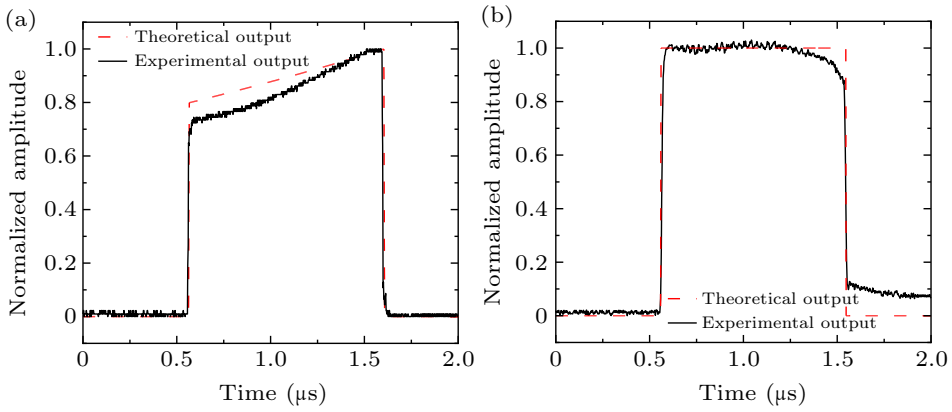


Fig. 3. Waveform shaping. Comparison between theoretically calculated and experimentally measured waveforms. (a) Comparison of the input waveform. (b) Comparison of the output waveform. The root-mean-square (RMS) deviation is 1% in the interval between 0.6 μs and 1.3 μs. All red curves represent theoretical waveforms, while all black curves represent experimental waveforms. The amplifier module is operated at a pump power of 3 W and a repetition rate of 2 kHz.

To correct the waveform distortion, we employ an input waveform pre-shaping scheme. Based on the established relationship between the input and output waveforms, the Frantz–Nodvik equation is inversely solved to obtain[25]

$$I_{s,0}(t) = \frac{I_{s,z}(t)}{1-(1-G_0(z))\exp\left(-J_{\text{sat}}^{-1}\int_0^t I_{s,z}(t')\,\mathrm{d}t'\right)}. \quad (3)$$

Substituting the target output waveform into Eq. (3) yields the theoretical pre-shaped waveform. The basic workflow of waveform pre-shaping and the corresponding experimental setup are illustrated in Figs. 2(b) and 2(c). In practice, the theoretical pre-shaped waveform is loaded into a function generator to pre-modulate the seed light entering the pulsed fiber amplifier. The amplified optical pulse is detected with a high-speed photodetector; the resulting waveform is converted into an electrical signal and recorded by an oscilloscope. The amplified output waveform obtained directly from the theoretical pre-shaping still deviates from the target waveform because the experimentally applied pre-shaped waveform is the radio-frequency (RF) waveform that drives the internal AOM, rather than the optical pulse itself. Since the actual modulated optical pulse cannot be measured directly, the pre-shaped input waveform is fine-tuned iteratively based on the measured output.[26]

The effectiveness of the pre-shaping scheme in suppressing output waveform distortion is illustrated here for a target 1 μs square pulse, as shown in Fig. 3. In Fig. 3(a), the red curve shows the theoretically pre-shaped waveform, while the black curve corresponds to the experimentally implemented waveform after fine-tuning. The measured output (black curve) agrees well with the theoretical output (red curve), with a root-mean-square (RMS) deviation of 1% over the interval between 0.6 μs and 1.3 μs, as shown in Fig. 3(b). Compared to the unshaped input, the pre-shaped waveform effectively suppresses the overall pulse distortion.

Although the output waveform distortion has been significantly reduced, it still deviates to some extent from an ideal square pulse. We attribute this discrepancy mainly to two factors. First, the waveform pre-shaping scheme we employed adjusts only a few key parameters to control the overall shape of the pre-modulated waveform, offering limited precision for capturing finer details.[26,27] Second, the pre-shaping approach is based on the Frantz–Nodvik equation, which inherently incorporates certain idealizations, such as neglecting nonlinear effects like stimulated Raman scattering (SRS)[28] and stimulated Brillouin scattering (SBS),[29] which are unavoidable in practical systems.

In addition, we tested square pulses under different pulsewidth and pump- power conditions. The results show that when varying the pulse width at a fixed pump power, the output waveform distortion characteristics remain highly consistent because they follow the same gain profile. Under a fixed pulse width, increasing the pump power raises the initial gain, extends the time required to enter the gain-saturation regime, and consequently intensifies the waveform distortion. In both scenarios, applying the waveform pre-shaping method effectively suppresses the distortion and yields square-pulse outputs that closely approximate the ideal shape.

3. Coherent Rydberg excitation of single atoms

We then apply the pre-shaped pulse to drive Rydberg excitations in an atom-array platform. First, a cloud of cold ^{87}Rb atoms is prepared in a magneto-optical trap (MOT). Subsequently, an 830 nm beam is phase-modulated by a spatial light modulator (SLM) and tightly focused through a high-numerical-aperture lens to form an optical tweezer array. The tweezer array overlaps spatially with the MOT and is capable of trapping up to 10×20 atoms. Individually loaded atoms are further cooled via polarization gradient cooling and adiabatic cooling, reaching a final temperature of approximately 7 μK. Atoms are then optically pumped into the $|F = 1, m_F = 0\rangle$ state and excited to a Rydberg state via a two-photon transition. Finally, fluorescence detection is used to measure the probability of atoms remaining in the ground state.

The relevant energy-level structure of the ^{87}Rb atom and the two-photon Rydberg excitation scheme are shown in Fig. 4(a). Atoms are excited from the state $|0\rangle = |F = 1, m_F = 0\rangle$ to the $60S_{1/2}$ Rydberg state via a two-photon process. Both the 420 nm and 1013 nm excitation beams are π-polarized, with an intermediate-state detuning of 1.69 GHz. The π-polarization of the Rydberg excitation light is adopted to facilitate the subsequent implementation of a magic-intensity optical trap scheme, ensuring that the required magnetic field direction is perpendicular to the excitation beam.[1,2] The 1013 nm light originates from a homemade cat-eye laser; most of the output serves as seed light for the pulsed fiber amplifier, while a small portion is coupled into an ultra-stable cavity for frequency stabilization, resulting in a linewidth of a few hundred hertz (Fig. 2(a)). The time sequence for Rydberg excitation and the method used to select a single 1013 nm pulse are shown in Fig. 4(b). To maintain stable population inversion in the gain medium and prevent runaway accumulation of nonlinear effects, the pulsed fiber amplifier is operated in a burst mode.[17] For Rydberg excitation, a single pulse is extracted from the burst using a TTL-controlled switch. When the TTL signal is high, the amplifier outputs a single pulse (pulse 2) for excitation; when low, it continues to deliver the original pulse burst (pulse 1). The 420 nm laser is generated by frequency-doubling an 840 nm source, and its frequency is stabilized to the same ultra-stable cavity as the 1013 nm laser. The Rydberg excitation geometry is shown in Fig. 4(c). Two counter-propagating beams are aligned to a selected row of four atoms spaced about 20 μm apart. At this spacing, interatomic interactions are negligible, allowing each atom to be excited independently. This configuration makes use of the uniformity of the excitation light while improving data acquisition efficiency.

To enable a direct comparison between the CW and pulsed schemes, the output of the pulsed amplifier is coupled into the pre-aligned 1013 nm delivery fiber via a free-space optical path. This configuration allows rapid switching between the pulsed and CW excitation schemes as needed. Accounting for coupling losses in the free-space interface, approximately 50% of the pulsed amplifier's power is available for excitation.

The 1013 nm Rydberg excitation pulse is generated using the pre-shaping scheme under conditions of 10 μs pulse duration, 3.5 W pump power, and a 2 kHz repetition rate, corresponding to a peak power of approximately 5 W from the pulsed fiber amplifier. Rabi oscillation is measured by scanning the duration of the 420 nm pulse. To minimize decoherence due to power fluctuations, the 420 nm pulse is positioned at the center of the flat region of the 1013 nm pulse, as shown in Fig. 4(b).[30] The power fluctuation between amplified 1013 nm Rydberg excitation pulses is approximately 2%, while that for the 420 nm excitation pulses is about 1%.

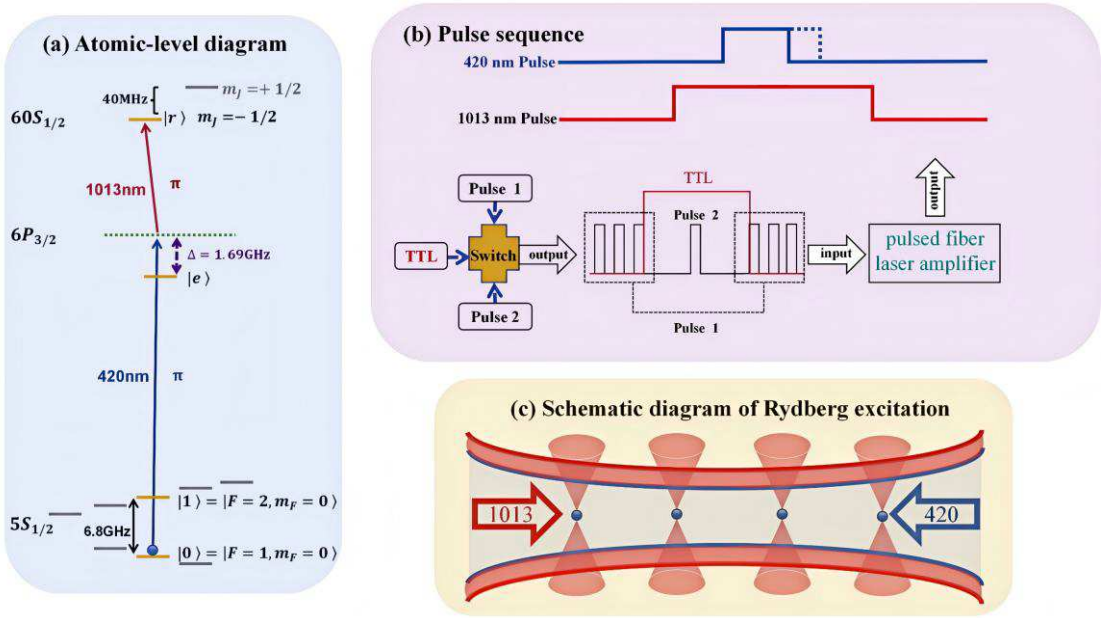


Fig. 4. Rydberg excitation scheme. (a) Main energy-level structure of ^{87}Rb. (b) Pulse sequence. A single 1013 nm pulse is selected from the pulse burst via a trigger-controlled switch for Rydberg excitation. The 420 nm pulse is positioned in the middle of the 1013 nm single pulse, and scanning the 420 nm pulse duration yields Rabi oscillations. (c) Rydberg excitation geometry. Both the 420 nm and 1013 nm beams are aligned in a counter-propagating configuration to a row of four atoms separated by approximately 20 μm.

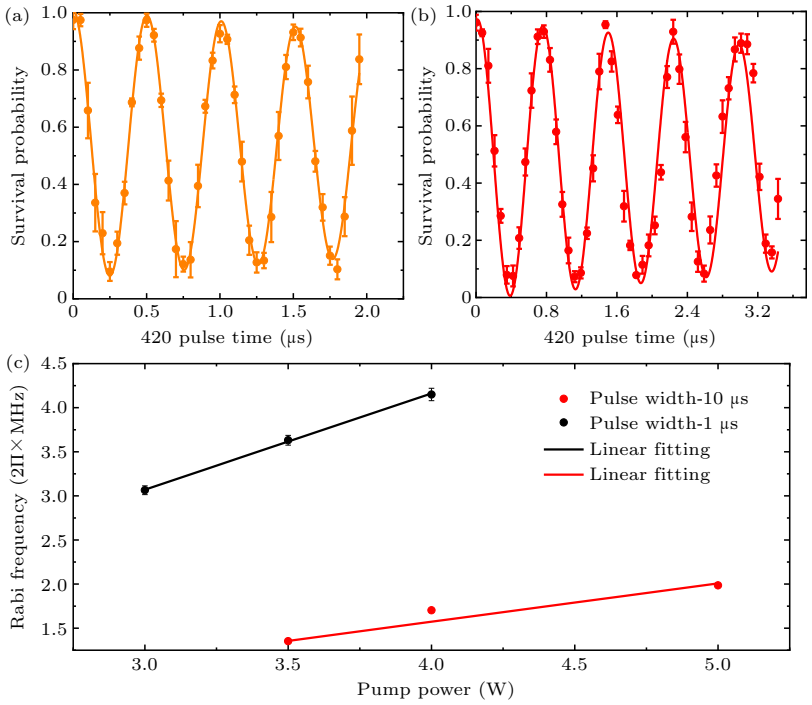


Fig. 5. Rabi oscillations between $|0\rangle$ and $|r\rangle$. (a) Rabi oscillation fringes using the conventional CW amplifier scheme. Fitting the experimental data (orange solid points) yields a two-photon Rabi frequency of $2\pi\times(1.98\pm0.01)$ MHz, and the $1/e$ decay time is 11.14 ± 3.62 μs. (b) Rabi oscillation fringes using the pulsed fiber amplifier scheme. Fitting the experimental data (red solid points) yields a two-photon Rabi frequency of $2\pi\times(1.35\pm0.01)$ MHz, and the $1/e$ decay time is 15.10 ± 7.54 μs. All these data points are averaged from 60 or 150 experimental measurements, and the error bar represents the standard deviation of the mean. (c) Rabi frequencies under different operating conditions of the pulsed fiber amplifier module.

We apply an external magnetic field to lift the degeneracy of the 60S state, splitting the m_j sublevels by approximately 40 MHz. By scanning the frequency of the 1013 nm excitation laser, we locate the absorption peak corresponding to the transition from the ground state to the Rydberg state $|r\rangle = |60S, m_j = -1/2\rangle$. With the 1013 nm laser tuned to resonance, we then scan the duration of the 420 nm pulse to drive coherent evolution between the ground and Rydberg states.

The Rabi oscillation between $|0\rangle$ and $|r\rangle$ obtained using the conventional CW scheme is shown in Fig. 5(a). A fit to the experimental data (orange solid points) yields a two-photon Rabi frequency of $2\pi\times(1.98\pm0.01)$ MHz, a $1/e$ lifetime of

11.14 ± 3.62 μs, and a contrast of ~ 0.94. The corresponding oscillation measured with the pulsed fiber amplifier scheme is shown in Fig. 5(b). Fitting the data (red solid points) yields a Rabi frequency of $2\pi \times (1.35 \pm 0.01)$ MHz, a $1/e$ lifetime of 15.10 ± 7.54 μs, and a contrast of ~ 0.98. Both schemes complete approximately 20 oscillation cycles within the $1/e$ lifetime, confirming their comparable coherence performance.

The pulsed fiber amplifier scheme enables the Rabi frequency to be increased directly by raising the pump power and shortening the pulse duration. To explore the performance limits of the amplifier module, we compare the achieved Rabi frequencies under different pump powers for two extreme pulse widths: 1 μs and 10 μs, and the results are shown in Fig. 5(c). Under the condition of a 1 μs pulse width, a 2 kHz repetition rate, and a pump power of 4 W, the pulsed fiber amplifier reaches its maximum output (~ 50 W peak power), yielding a two-photon Rabi frequency of $2\pi \times (4.25 \pm 0.06)$ MHz.

To evaluate potential linewidth broadening introduced by the pulsed amplifier, we perform Ramsey interferometry between $|0\rangle$ and $|r\rangle$ using a $\pi/2$-gap-$\pi/2$ pulse sequence. The results for the conventional CW scheme and the pulsed fiber amplifier scheme are compared in Fig. 6. For the pulsed fiber amplifier scheme, the fitted dephasing time extracted from the Ramsey fringes is $T_2^* = 5.25 \pm 0.78$ μs (Fig. 6(b)). At a temperature of $T = 7$ μK, the random shot-to-shot variation in atomic velocity results in a Gaussian-distributed Doppler detuning $\delta_D/(2\pi)$, corresponding to an expected dephasing time of 6.24 μs. This indicates that the dephasing is dominated by thermal Doppler effects. The measured dephasing time for the pulsed fiber amplifier scheme is comparable to the value of 6.42 ± 0.73 μs obtained with the CW scheme. Currently, the $\sim 2\%$ shot-to-shot power fluctuations of the 1013 nm pulsed output are about twice those of the CW source; improving this stability could further extend the dephasing time.[31] These results indicate that the MOPA architecture largely preserves the narrow linewidth of the seed laser during power amplification, thus enabling efficient coherent control of Rydberg atoms.

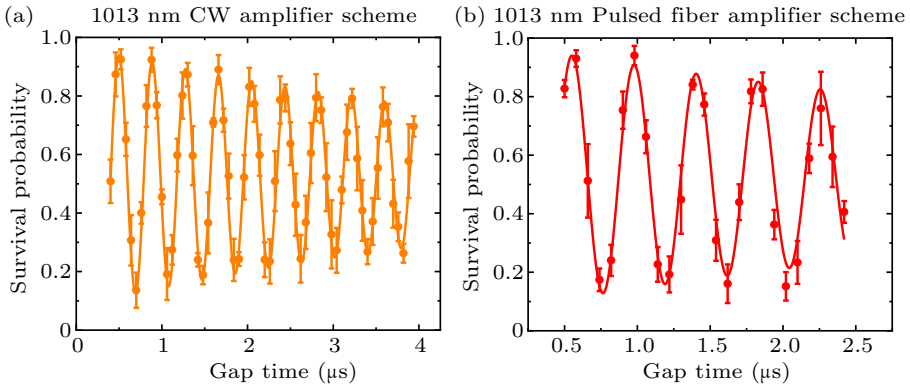


Fig. 6. Ramsey fringes between $|0\rangle$ and $|r\rangle$. (a) Ramsey fringes using the CW amplifier scheme. The data points (orange) are fitted to an exponentially decaying sine curve (orange) with a $1/e$ decay time of 6.42 ± 0.73 μs. (b) Ramsey fringes using the pulsed fiber amplifier scheme. The data points (red) are fitted to an exponentially decaying sine curve (red) with a $1/e$ decay time of 5.25 ± 0.78 μs. All these data points are averaged from 60 single experimental measurements, and the error bar represents the standard deviation of the mean.

4. Conclusion and outlook

This study demonstrates efficient coherent Rydberg excitation of single atoms using a fiber-based MOPA system, achieving performance comparable to CW excitation. The MOPA architecture provides a promising route to deliver higher peak power while preserving the spectral quality of the seed laser. The Rydberg Rabi frequency can be flexibly tuned through pump power and pulse width adjustments, potentially exceeding the coupling strength achievable with conventional CW lasers. This approach provides a scalable route to large-scale quantum simulation and computation based on Rydberg atom arrays.

In the future, closed-loop feedback[32,33] could further improve the amplified output waveform quality and enable arbitrary waveform generation. Such capabilities would be suitable for single off-resonant modulated pulse schemes[34–36] aimed at high-fidelity two-qubit gates. For these implementations, controlling the phase noise introduced during amplification — which has not been systematically examined here — remains an important task[37,38] and offers a compelling direction for further study. Furthermore, the high-repetition-rate, short-pulse burst generated by the amplifier module is naturally suited for periodically driving quantum systems, enabling the study of novel nonequilibrium phenomena such as discrete time crystals.[39,40]

Acknowledgments

Project supported by the National Key Research and Development Program of China (Grant No. 2021YFA1402001), the National Natural Science Foundation of China (Grant Nos. 12261131507 and 12074391), the Natural Science Foundation of Wuhan (Grant No. 2024040701010063), and the Major Program (JD) of Hubei Province (Grant

No. 2023BAA020).

References

[1] Yang J H, He X D, Guo R J, Xu P, Wang K P, Sheng C, Liu M, Wang J, Derevianko A and Zhan M S 2016 *Phys. Rev. Lett.* **117** 123201

[2] Guo R J, He X D, Sheng C, Yang J H, Xu P, Wang K P, Zhong J Q, Liu M, Wang J and Zhan M S 2020 *Phys. Rev. Lett.* **124** 153201

[3] Manetsch H J, Nomura G, Bataille E, Lv X, Leung K H and Endres M 2025 *Nature* **647** 60

[4] Wang Y Q, Liao Y X, Zhang T, Tian Y, Wu Y J, Zhang W J, Zhang W, Huang Y D, Zhai H, Chen W L, Feng X and Zhang Z C 2026 *Chin. Phys. Lett.* **43** 10606

[5] Bluvstein D, Levine H, Semeghini G, Wang T T, Ebadi S, Kalinowski M, Keesling A, Maskara N, Pichler H, Greiner M, Vuletić V and Lukin M D 2022 *Nature* **604** 451

[6] Madjarov I S, Covey J P, Shaw A L, Choi J, Kale A, Cooper A, Pichler H, Schkolnik V, Williams J R and Endres M 2020 *Nat. Phys.* **16** 857

[7] Fu Z, Xu P, Sun Y, Liu Y Y, He X D, Li X, Liu M, Li R B, Wang J, Liu L and Zhan M S 2022 *Phys. Rev. A* **105** 42430

[8] Evered S J, Bluvstein D, Kalinowski M, Ebadi S, Manovitz T, Zhou H Y, Sophie H L, Alexandra A G, Wang T T, Maskara N, Levine H, Semeghini G, Greiner M, Vuletić V and Lukin M D 2023 *Nature* **622** 268

[9] Radnaev A G, Chung W C, Cole D C, *et al.* 2025 *PRX Quantum* **6** 30334

[10] Scholl P, Schuler M, Williams H J, Eberharter A A, Barredo D, Schymik K N, Lienhard V, Henry L P, Lang T C, Lahaye T, Läuchli A M and Browaeys A 2021 *Nature* **595** 233

[11] Ebadi S, Wang T T, Levine H, Keesling A, Semeghini G, Omran A, Bluvstein D, Samajdar R, Pichler H, Ho W W, Choi S, Sachdev S, Greiner M, Vuletić V and Lukin M D 2021 *Nature* **595** 227

[12] Semeghini G, Levine H, Keesling A, Ebadi S, Wang T T, Bluvstein D, Verresen R, Pichler H, Kalinowski M, Samajdar R, Omran A, Sachdev S, Vishwanath A, Greiner M, Vuletić V and Lukin M D 2021 *Science* **374** 1242

[13] Bluvstein D, Evered S J, Geim A A, *et al.* 2024 *Nature* **626** 58

[14] Bluvstein D, Geim A A, Li S H, *et al.* 2026 *Nature* **649** 39

[15] Preskill J 2018 *Quantum* **2** 79

[16] Fan H 2018 *Acta Phys. Sin.* **67** 120301 (in Chinese)

[17] Zervas M N and Codemard C A 2014 *IEEE J. Sel. Top. Quantum Electron.* **20** 219

[18] Li C Y, Ye L, Li C, Li Q S, Zhang Z Q, Sun X P, Zang Y N, Han S, Xu L and Shi J F 2020 *Optik* **223** 165415

[19] Yu G L, Ding J Y, Fang C Q, Li B B, Qian Y, Zhou J, Chen W B and Zhu X L 2023 *Opt. Commun.* **545** 129718

[20] Mahesh T P, Matsubara T, Chew Y T, Tomita T, Léséleuc S D and Ohmori K 2025 *Opt. Lett.* **50** 403

[21] Cai T, He J, Liu Z H, Liu Y, Su N, Shi P F, Jin G, Cheng Y J and Wang J M 2025 *Acta Phys. Sin.* **74** 13201 (in Chinese)

[22] Paschotta R, Nilsson J, Tropper A C and Hanna D C 1997 *IEEE J. Quantum Electron.* **33** 1049

[23] Frantz L M and Nodvik J S 1963 *J. Appl. Phys.* **34** 2346

[24] Luo X, Tang Y T, Dong F L, Wang J C, Yu L P, Yan P G, Wang J Z, Lue Q T, Guo C Y and Ruan S C 2023 *Opt. Lett.* **48** 1790

[25] Schimpf D N, Ruchert C, Nodop D, Limpert J, Tünnermann A and Salin F 2008 *Opt. Express* **16** 17637

[26] Vu K T, Malinowski A, Richardson D J, Ghiringhelli F, Hickey L M B and Zervas M N 2006 *Opt. Express* **14** 10996

[27] Xu S, Zou S Z, Yu H J, Zuo J X, Ning C Y, Chen X C, Li X Y, Wu W J and Lin X C 2024 *Opt. Express* **32** 9397

[28] Stolen R H, Ippen E P and Tynes A R 1972 *Appl. Phys. Lett.* **20** 62

[29] Kobyakov A, Sauer M and Chowdhury D 2010 *Adv. Opt. Photonics* **2** 1

[30] Léséleuc S D, Barredo D, Lienhard V, Browaeys A and Lahaye T 2018 *Phys. Rev. A* **97** 53803

[31] Liu Y Y, Sun Y, Fu Z, Xu P, Wang X, He X D, Wang J and Zhan M S 2021 *Phys. Rev. Appl.* **15** 54020

[32] Oliveira P, Addis S, Gay J, Ertel K, Galimberti M and Musgrave I 2019 *Opt. Express* **27** 6607

[33] Yang S Z, Masella, Moeini V, Bellahsene A, Li C, Bienaimé T and Whitlock S 2025 *Phys. Rev. Appl.* **23** 054009

[34] Sun Y 2023 *Phys. Rev. Appl.* **20** L061002

[35] Sun Y, Xu P, Chen P X and Liu L 2020 *Phys. Rev. Appl.* **13** 24059

[36] Jandura S and Pupillo G 2022 *Quantum* **6** 712

[37] de Vries O D, Plötner M, Christaller F, Zhang H, Belz A, Heinrich B, Kübler H, Löw R, Pfau T, Walbaum T, Schreiber T and Tünnermann A 2020 *Opt. Express* **28** 17362

[38] Sheng Q, Wang M, Shi C D, Tian H, Zhang J X, Liu J J, Shi W and Yao J Q 2021 *Acta Phys. Sin.* **70** 214202 (in Chinese)

[39] Fan C H, Rossini D, Zhang H X, Wu J H, Artoni M and La Rocca G C L 2020 *Phys. Rev. A* **101** 13417

[40] Wang J J, Tang L Z, Du Y X and Zhang D W 2025 *Phys. Lett. A* **558** 130896